

POLITECNICO DI TORINO
Repository ISTITUZIONALE

Drift Rejection Differential Frontend for Single Plate Capacitive Sensors

Original

Drift Rejection Differential Frontend for Single Plate Capacitive Sensors / Subbicini, Giorgia; Lavagno, Luciano; Lazarescu, Mihai T.. - In: IEEE SENSORS JOURNAL. - ISSN 1530-437X. - ELETTRONICO. - 22:16(2022), pp. 16141-16149. [10.1109/JSEN.2022.3189031]

Availability:

This version is available at: 11583/2970213 since: 2022-11-17T16:40:31Z

Publisher:

IEEE

Published

DOI:10.1109/JSEN.2022.3189031

Terms of use:

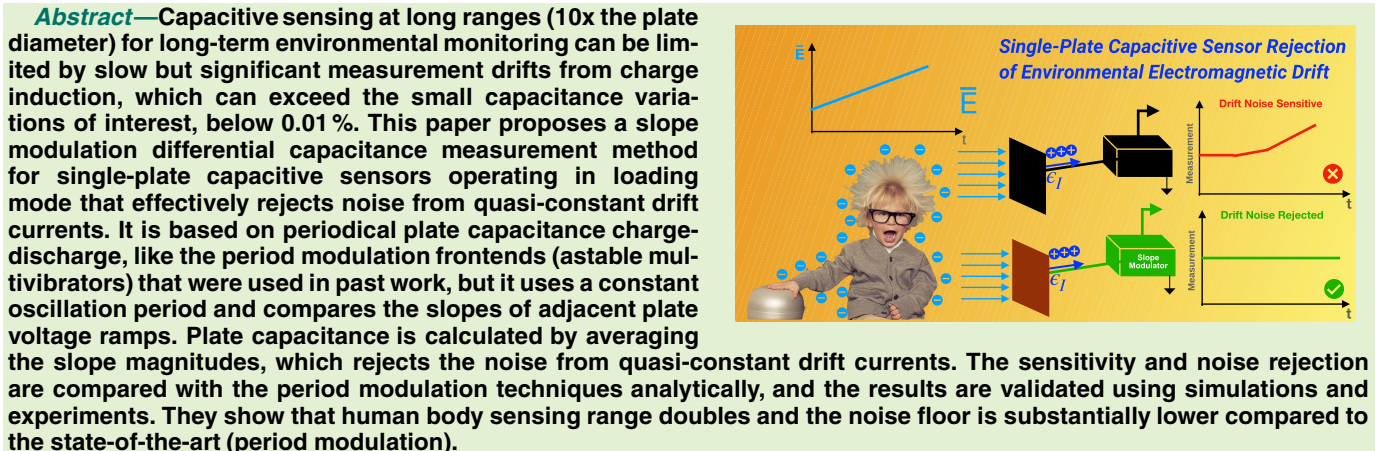
This article is made available under terms and conditions as specified in the corresponding bibliographic description in the repository

Publisher copyright

(Article begins on next page)

Drift Rejection Differential Frontend for Single Plate Capacitive Sensors

Giorgia Subbicini^{ID}, Member, IEEE, Luciano Lavagno^{ID}, Senior Member, IEEE,
and Mihai T. Lazarescu^{ID}, Senior Member, IEEE



Index Terms—Capacitive sensor, differential measurement, drift rejection, noise reduction, environmental monitoring.

I. INTRODUCTION

CAPACITIVE sensors find many applications, e.g., for human-machine interfaces [1], measurement [2], or sensing [3], [4]. They can cover from very large surfaces down to nanostructures [5], [6], and many sensing needs from gas detectors, to tomography and defectoscopy [7]–[9], with low cost and low power consumption.

At longer sensing ranges (e.g., 10 times the plate diameter), small capacitive sensors find applications for inconspicuous low power low cost indoor person localization or identification [10]–[12] for home automation or assisted living [13], [14]. However, at long ranges the measurement field cannot be effectively protected from drift and noise [15], [16]. Thus, measurement stability and accuracy can be affected by various environmental conditions. This is even more noticeable because the capacitance variations of interest are very small at long sensing ranges, below 0.01% [11], [17].

Manuscript received 19 March 2022; revised 27 May 2022 and 4 July 2022; accepted 4 July 2022. Date of publication 13 July 2022; date of current version 15 August 2022. The associate editor coordinating the review of this article and approving it for publication was Dr. Ferran Reverter. (*Corresponding author: Giorgia Subbicini.*)

The authors are with the Electronics and Telecommunications Department, Politecnico di Torino, 10129 Torino, Italy (e-mail: giorgia.subbicini@polito.it; luciano.lavagno@polito.it; mihai.lazarescu@polito.it).

Digital Object Identifier 10.1109/JSEN.2022.3189031

Slow measurement drift cannot be effectively filtered in long term monitoring applications of stationary or slow changing scenarios, and it can often limit the effectiveness of long range capacitive sensing. Drift can come from actual capacitance changes, e.g., because of variable air humidity, which can be compensated. Other causes, which we will address, are changes in the environmental conditions which affect the operation of the sensor frontend without changing the sensor capacitance.

Period modulation frontends are often used to measure the sensor plate capacitance. Tan *et al.* [18] propose self-calibration and several trade-offs to significantly reduce the power consumption of the frontend for long-term monitoring using wireless sensor networks. An astable multivibrator circuit for wide range capacitance measurements is proposed in [19] using a Schmitt trigger with adjustable thresholds. A period modulation frontend for capacitive sensors for sub-nanometer displacement measurement, which uses chopping, self-calibration, and active shielding to reduce errors is proposed in [20]. In our previous work [21], a simple period modulation frontend based on a 555 timer is used, that is highly susceptible to environmental noise, to acquire capacitive sensor measurements for person localization using machine learning. Differential measurement methods were also proposed. A direct interface, using only passive components, is proposed in [22] with 1% full scale accuracy, and

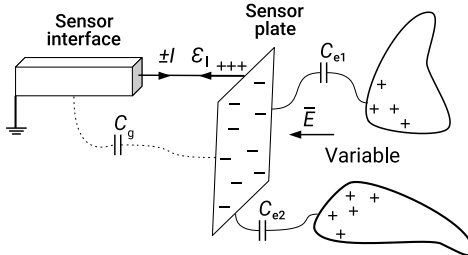


Fig. 1. Single-plate capacitive sensor model with measurement frontend, main capacitances, drive current I and drift current ε_I from charge induction in variable environmental electromagnetic fields.

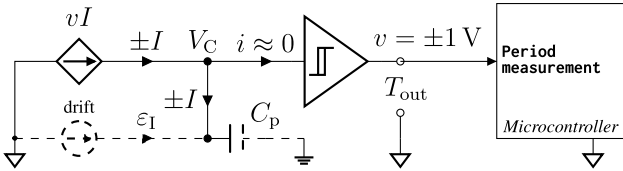


Fig. 2. Period modulation frontend block schematic with the drift current ε_I modeling the charge induction of the sensor plate mutual capacitance C_p with surrounding objects of different electrical potentials.

a method based on dual ramp integrator is proposed in [23] with errors below 0.2%.

Existing works address mostly the measurement of lumped capacitors or are applied to short range sensing in controlled environmental conditions. In this paper instead environmental influences on single plate long range capacitive sensors for environmental monitoring are taken in examination, which form capacitances with bodies around them using unprotected measurement fields. First, a full analysis is performed on the noise induced by variable environmental electric fields on period modulation frontends. Second, a new frontend based on slope modulation and differential measurements are proposed, that can effectively reject noise from slow drifts, while preserving the capacitance measurement sensitivity.

II. SENSOR DRIFT PROBLEM

The electrical capacitance C of an object is defined as the ratio between the variation of its electrical charge, ΔQ , and the corresponding variation of its electrical potential, ΔV_C

$$C = \frac{\Delta Q}{\Delta V_C}. \quad (1)$$

While the capacitance is fully defined by the electric and dielectric properties and geometries [24], the measurement frontends can instead be susceptible to several other environmental influences, e.g., from electromagnetic fields.

Fig. 1 shows the operating principle of a period modulation frontend for single-plate capacitance sensors. The sensor plate forms capacitances with bodies in the environment (C_{e1} , C_{e2} , ...) and with nearby objects, such as the frontend circuits and the ground (C_g). Period modulation frontends, with the block schematic shown in Fig. 2, cyclically charge and discharge the sensor plate with a constant current I measuring the variation of its potential V_C against a fixed reference. The plate potential is defined by the electric charge density σ on

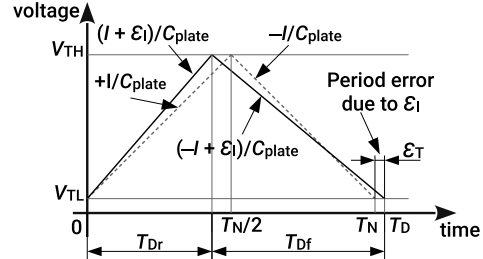


Fig. 3. Period modulation frontend errors due to the drift current, ε_I .

the plate surface, S_{plate} , which balances the electric flux Φ_E from the environmental electric field \mathbf{E} on the same surface

$$\sigma = \Phi_E, \quad \Phi_E = \int_{S_{plate}} \mathbf{E} \cdot d\mathbf{S}. \quad (2)$$

E variations change σ , hence induce currents ε_I [24] that add algebraically to the frontend driver current I . Here we focus mostly on the slow, quasi-constant \mathbf{E} variations, e.g., created during the dispersion of environmental charge buildups, and on measuring frontend rejection of the noise from the induced drift currents, ε_I . Significant charge can accumulate during common industrial or home activities, e.g., walking on carpeted floors can generate electrostatic voltages up to 15 kV [25].

Period modulation constant-current frontends (see Fig. 2) repeatedly charge-discharge the mutual plate capacitance C_p (made with the surrounding objects) with a current $\pm I$ from a constant current source, or an exponential current from a voltage source through a resistor. Under constant current I , the plate voltage V_C changes linearly (see the dashed plot in Fig. 3)

$$C_p = \frac{I \Delta t}{\Delta V_C}, \quad \Delta V_C = \frac{I}{C_p} \Delta t. \quad (3)$$

When V_C reaches the thresholds of a hysteresis comparator (V_{TL} , V_{TH}), the sign of the current I changes to satisfy $V_{TL} \leq V_C \leq V_{TH}$. With constant C_p and no noise, the charge and discharge times are identical

$$C_p \frac{V_{TH} - V_{TL}}{I} = C_p \frac{V_{TL} - V_{TH}}{-I} = \frac{T_N}{2}, \quad (4)$$

C_p can be calculated from the oscillation period T_N

$$C_p = \underbrace{\frac{I}{2(V_{TH} - V_{TL})}}_{\text{constant}} T_N. \quad (5)$$

and the sensitivity of the output frequency to changes of C_p is

$$\frac{\partial f_N}{\partial C_p} = -\frac{I}{2(V_{TH} - V_{TL})} \cdot \frac{1}{C_p^2}, \quad f_N = \frac{1}{T_N}. \quad (6)$$

However, as shown in Fig. 3, an external quasi-constant drift current ε_I unbalances the durations of the rising T_{Dr} and falling T_{Df} ramps. From (4) we have

$$T_{Dr} = C_p \frac{V_{TH} - V_{TL}}{I + \varepsilon_I}, \quad T_{Df} = C_p \frac{V_{TL} - V_{TH}}{-I + \varepsilon_I} \quad (7)$$

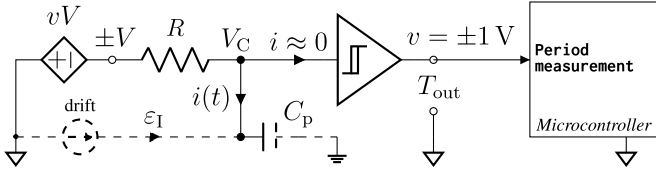


Fig. 4. RC period modulation frontend block schematic with the drift current ε_I modeling the charge induction of the sensor plate mutual capacitance C_p with surrounding objects of different electrical potentials.

and the oscillation period T_D becomes

$$T_D = T_{DR} + T_{DF} = 2(V_{TH} - V_{TL}) \underbrace{\frac{I}{I^2 - \varepsilon_I^2}}_{\text{not constant}} C_p. \quad (8)$$

The relative period error is obtained from (5) and (8)

$$\varepsilon_T = \frac{T_D - T_N}{T_N} = \frac{\varepsilon_I^2}{I^2 - \varepsilon_I^2}. \quad (9)$$

Hence, a constant drift current ε_I always increases the oscillation period T_D of the frontend, leading to measurement errors when calculating C_p using (5).

The oscillation period of period modulating frontends using RC astable multivibrators, rather than based on constant currents, is affected by similar errors. The block schematic in Fig. 4 shows how the frontend charges and discharges the plate capacitance C_p between the voltage thresholds of a hysteresis comparator through a resistor R from two constant dc voltages, $\pm V$. The charging current $i(t)$ is

$$i(t) = \frac{V - V_C(t)}{R}, \quad \frac{dV_C(t)}{dt} = \frac{i(t)}{C_p} = \frac{V - V_C(t)}{R C_p}. \quad (10)$$

Solving for V_C we obtain the well-known RC charge expression

$$V_C(t) = (V_{TL} - V)e^{-\frac{t}{\tau}} + V, \quad \tau = R C_p \quad (11)$$

where V_{TL} is the voltage of the lowest threshold of the hysteresis comparator and V is the source (charging) voltage.

Assuming distinct dc voltages for charging, V_H , and discharging, V_L , the charging, T_{Nr} , and the discharging, T_{Nf} , times are

$$T_{Nr} = -\tau \ln \frac{V_{TH} - V_H}{V_{TL} - V_H} \quad (12)$$

$$T_{Nf} = -\tau \ln \frac{V_{TL} - V_L}{V_{TH} - V_L} \quad (13)$$

and the noise-free oscillation period is

$$T_N = T_{Nr} + T_{Nf} = -\tau \ln \frac{(V_{TH} - V_H) \cdot (V_{TL} - V_L)}{(V_{TL} - V_H) \cdot (V_{TH} - V_L)} = -\tau \ln \frac{K_a}{K_b} \quad K_a < 0, \quad K_b < 0. \quad (14)$$

An induced quasi-constant drift current ε_I (see Fig. 4) algebraically adds to $i(t)$ in (10). During charging we have

$$\frac{dV_C(t)}{dt} = \frac{\frac{V_H - V_C(t)}{R} + \varepsilon_I}{C_p} = \frac{V_H - V_C(t) + \varepsilon_V}{R C_p}, \quad \varepsilon_V = R \varepsilon_I \quad (15)$$

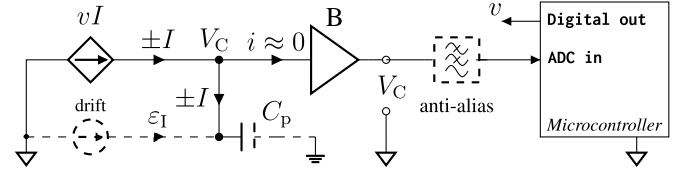


Fig. 5. Slope modulation frontend block schematic with the drift current ε_I modeling the charge induction of the sensor plate mutual capacitance C_p with surrounding objects of different electrical potentials.

and solving for V_C

$$V_C(t) = (V_{TL} - V_H - \varepsilon_V)e^{-\frac{t}{\tau}} + V_H + \varepsilon_V. \quad (16)$$

Thus, the charging, T_{DR} , and the discharging, T_{DF} , times considering a quasi-constant drift current ε_I are

$$T_{DR} = -\tau \ln \frac{V_{TH} - V_H - \varepsilon_V}{V_{TL} - V_H - \varepsilon_V}, \quad (17)$$

$$T_{DF} = -\tau \ln \frac{V_{TL} - V_L - \varepsilon_V}{V_{TH} - V_L - \varepsilon_V}, \quad (18)$$

the frontend oscillation period is

$$T_D = T_{DR} + T_{DF} = -\tau \ln \left(\frac{V_{TH} - V_H - \varepsilon_V}{V_{TL} - V_H - \varepsilon_V} \cdot \frac{V_{TL} - V_L - \varepsilon_V}{V_{TH} - V_L - \varepsilon_V} \right) = -\tau \ln \frac{|K_a| - \varepsilon_V^2}{|K_b| - \varepsilon_V^2}, \quad (19)$$

and the relative oscillation period error due to drift current ε_I

$$\varepsilon_T = \frac{T_D - T_N}{T_N} = \frac{\ln \frac{|K_a| - \varepsilon_V^2}{|K_b| - \varepsilon_V^2}}{\ln \frac{|K_a|}{|K_b|}} - 1 = \frac{\ln \frac{|K_a|}{|K_b|} - \frac{\varepsilon_V^2}{|K_b|}}{\ln \frac{|K_a|}{|K_b|}}. \quad (20)$$

In a first approximation, $\varepsilon_T \propto \ln(1 - \varepsilon_I^2)$ (since $\varepsilon_V = R \varepsilon_I$), higher than for constant current period modulation frontends.

III. DRIFT REJECTION METHOD

The operation of the proposed slope modulation frontend shown in Fig. 5 is similar to the period modulation frontend shown in Fig. 2. The timing of the charge-discharge cycles is constant because we use the ramp slopes for C_p calculation, which allows to better reject drift noise.

The V_C ramp slope S is inversely proportional to C_p in (3)

$$S = \frac{\Delta V_C}{\Delta t} = \frac{I}{C_p}. \quad (21)$$

and a constant drift current ε_I changes both the rising S_r and the falling S_f slopes

$$S_r = \frac{I + \varepsilon_I}{C_p}, \quad S_f = \frac{-I + \varepsilon_I}{C_p}. \quad (22)$$

But the average of the slope magnitudes, S_a , is invariant to ε_I

$$S_a = \frac{|S_r| + |S_f|}{2} = \frac{1}{2} \left(\frac{I + \varepsilon_I}{C_p} - \frac{-I + \varepsilon_I}{C_p} \right) = \frac{I}{C_p}. \quad (23)$$

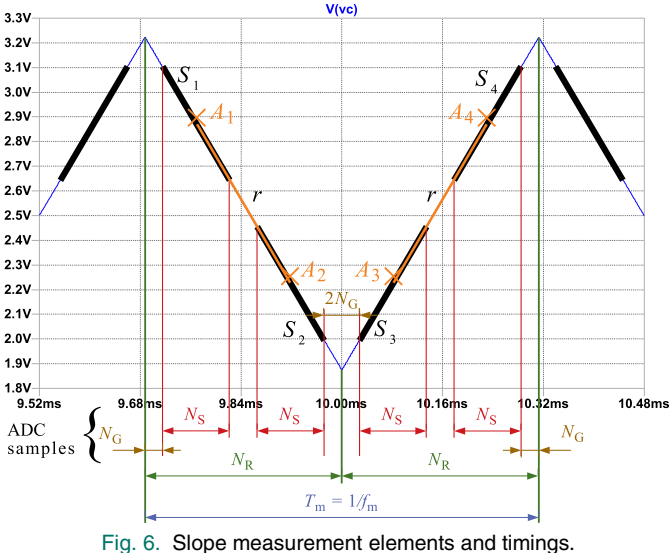


Fig. 6. Slope measurement elements and timings.

Moreover, the measurement sensitivity to C_p is comparable with the period modulation frontend in (6)

$$\frac{\partial S_a}{\partial C_p} = -\frac{I}{C_p^2}. \quad (24)$$

Hence, by measuring the slope of two adjacent charge-discharge ramps we can calculate C_p using (23) and reject as common mode signals the errors from quasi-constant drift currents, ε_I , as from other drift sources, e.g., flicker ($1/f$) noise.

Importantly, drift rejection depends on how well the constant ε_I (and noise in general) is matched on two adjacent ramps, and on the component nonlinearities and value mismatches.

A. Measurement Method

Fig. 6 shows the main elements used to measure the slopes of the charge-discharge ramps to calculate C_p using (23). The measurement period T_m is accurately set by a microcontroller (signal v in Fig. 5), and should be at most half of the shortest sensor signal period according to the Nyquist-Shannon sampling theorem [26]. T_m is synchronized with an analog-to-digital converter (ADC) that acquires N_R samples of V_C on each ramp. The voltages V_A of two A points must be determined to calculate the slope of each ramp. Each A is the midpoint of an N_S sample segment S . To lower the quantization noise through oversampling and decimation [27], we optimize N_S to a power of four

$$V_{A_i} = \frac{1}{N_S} \sum_{j=1}^{N_S} V_{S_{i,j}}, \quad i \in \{1, 2, 3, 4\}, \quad N_S = 4^n, \quad n \in \mathbb{N} \quad (25)$$

where V_{S_i} are the samples of the N_S ramp in the segment S_i .

Note that the frontend in Fig. 5 controls only the amplitude of V_C , through the current I and the period T_m , but not its absolute value. Circuit asymmetries or environmental effects may accumulate over time and bring V_C partly into the frontend nonlinearity region, which may distort its extremes. Anti-aliasing filters (see Fig. 5) may also distort the V_C ramp

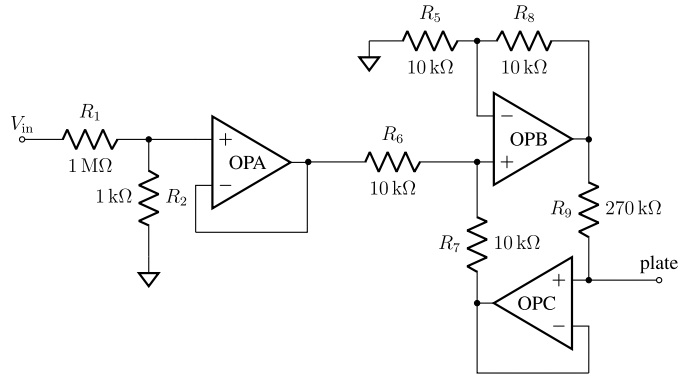


Fig. 7. Improved Howland current source modeling the noise current.

ends. Hence, for better measurement accuracy the segments S must be long and well spaced, but also far enough from the ramp ends to skip distortions (N_G skipped samples in Fig. 6).

The time between the two A points on each ramp is

$$T_{A_{1,2}} = T_{A_{3,4}} = \frac{T_m}{2N_R} \left[N_R - 2 \left(N_G + \frac{N_S}{2} \right) \right]. \quad (26)$$

Eq. (26), (21) give the rising, S_r , and falling, S_f , ramp slopes

$$S_r = \frac{2N_R (V_{A_4} - V_{A_3})}{T_m (N_R - 2N_G - N_S)}, \quad S_f = \frac{2N_R (V_{A_2} - V_{A_1})}{T_m (N_R - 2N_G - N_S)} \quad (27)$$

then we obtain C_p from (23)

$$C_p = \frac{I T_m}{V_{A_4} - V_{A_3} - (V_{A_2} - V_{A_1})} \cdot \frac{N_R - 2N_G - N_S}{N_R}. \quad (28)$$

Hence, from the frontend design parameters I , T_m , N_R , N_S , N_G and the voltages V_A of midpoints A of the acquisition segments S we can calculate the plate capacitance C_p .

IV. SIMULATION AND EXPERIMENTAL TESTING

Plate capacitance slow measurement drifts may indicate actual capacitance variations (e.g., due to changes of air humidity), or measurement interface errors upon changes of measurement conditions (e.g., charge induction currents from variable environmental electric fields from charge buildup or leakage). While the former variations can be usually independently measured and compensated, the latter can hardly be detected and the measurement interface should be intrinsically insensitive.

In Section II the slope modulation measurement interface rejection capability of the low frequency drift currents is analytically demonstrated. Here analytic results are validated through simulations and laboratory experiments for drift currents at different frequencies.

For grounded capacitors [28], changes of electrical potential of the grounded plate (surrounding objects in our case) often determine charge induction currents. Because mutual plate capacitance and relatively large voltage variations are hard to produce and control, the charge induction current is injected directly into the sensor plate node using a voltage-controlled current source (see Fig. 7).

The slope modulation frontend (see Fig. 5 and Fig. 8) uses a high input impedance differential amplifier made of

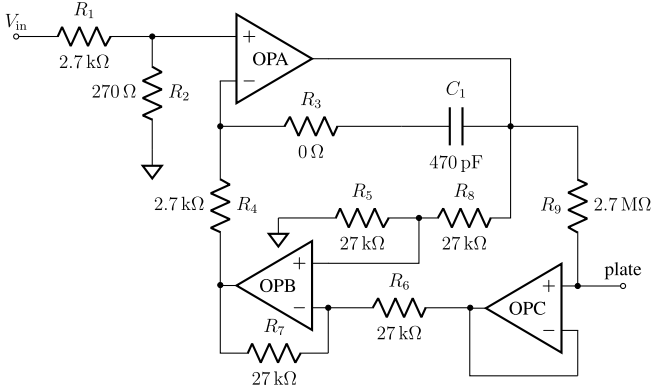


Fig. 8. Schematic of the slope modulation frontend.

operational amplifiers OPB and OPC to measure the voltage across the current sensing resistor R_9 . The result drives the OPA inverting input, while its non-inverting input is set to the constant reference voltage driven by a microcontroller through the R_1-R_2 voltage divider. Thus, the current through R_9 (hence through C_p) is

$$I = \frac{(V_{in} - 1.65 \text{ V}) \frac{R_2}{R_1+R_2} + 1.65 \text{ V}}{R_9}, \quad (29)$$

where V_{in} is a digital output assuming either 0 V (logic low) or supply voltage, 3.3 V (logic high). The same current source is used also for the constant current period modulation frontend.

The RC period modulation frontend uses an exponential current limited by a resistor R . Moreover, for the typically small C_p , practical R values increase the average current well beyond the constant current of the other two frontends.

A. Testing Parameters

The sensor plate capacitance is modeled with a constant $C_p = 10 \text{ pF}$ capacitor connected to the ground, comparable to the $16 \text{ cm} \times 16 \text{ cm}$ plate self-capacitance of the prototype.

The parameters of the slope modulation front-end (see Fig. 8) are set as discussed in Section III-A. The measurement period T_m (see Fig. 6) must be long for the ADC to acquire many N_R samples per ramp (to increase accuracy and reduce quantization noise), yet short enough to keep V_C swings within OPA input limits. V_C swings also depend on the charge/discharge current magnitude, I . Thus, low C_p requires low I . But since I is set mainly by (see Fig. 5) the voltage divider R_1 , R_2 and by R_9 value (29), the output voltage of the divider must be much higher than the OPA input voltage offset for low errors, and R_9 value is capped by practical values and to keep the driving impedance of the plate node relatively low, less susceptible to noise. Yet R_9 cannot be too low, because higher I values tend to decrease measurement sensitivity (24), as shown in Fig. 9.

The STM32L412 [29] low-power low-cost general purpose microcontroller board is selected to drive the prototype frontend. It provides sufficient onboard memory and processing power, a 5Msample/s ADC, and a regulated 3.3 V supply. It plugs into the frontend (see Fig. 10) keeping the high sensitivity analog circuits distant and shielded from the noisy digital parts.

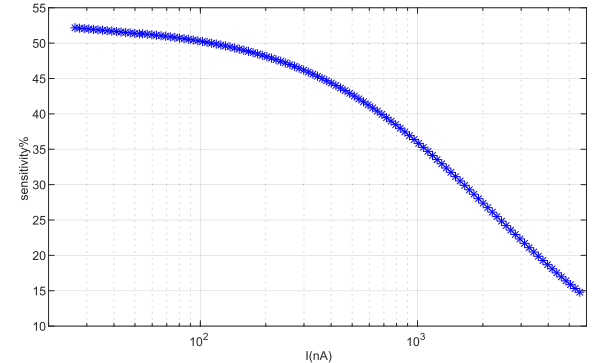


Fig. 9. Slope modulator sensitivity with the magnitude of the constant current I which charges/discharges the sensor plate.

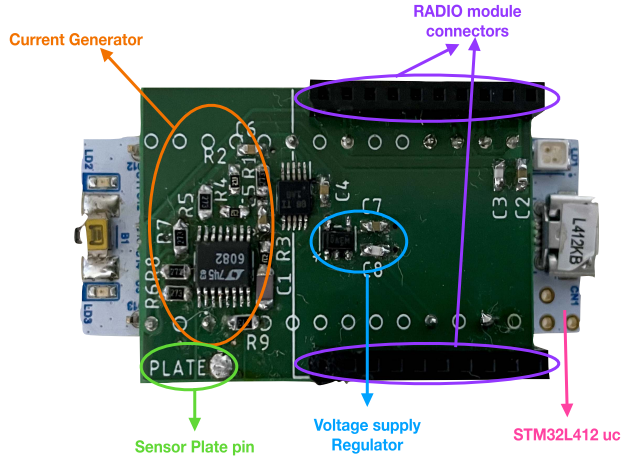


Fig. 10. PCBs assembly of the slope modulation interface (top) with the STM32L412 microcontroller board (bottom).

TABLE I
SLOPE MODULATION FRONTEND POSSIBLE MEASUREMENT
FREQUENCIES ($1/T_m$) FOR 2 MSAMPLE/S SAMPLING RATE,
OVERSAMPLING BITS (n), UNUSED SAMPLES PER RAMP ($2N_G + r$)
AND THEIR PERCENTAGE OF TOTAL, AND PLATE CAPACITANCE
VOLTAGE SWING (V_C) FOR $I = 40 \text{ nA}$

Measurement frequency (Hz)	Oversampling (bit)	Unused samples per ramp	Ramp coverage (%)	V_C amplitude ($I = 40 \text{ nA}$) (V)
1600	4	113	82	1.25
6250	3	32	80	0.32
5000	3	72	64	0.4
1250	4	288	64	1.6
4000	3	122	52	0.5
1000	4	488	52	2.0

ADC acquisition is set at 2Msample/s, more available on low-end microcontrollers. Table I lists, with the considerations above and in Section III-A, the T_m periods using at least half of the ADC samples, the resolution bits n gained from oversampling, and the peak-to-peak V_C for $I = 40 \text{ nA}$. An integer number of ADC samples per ramp (see Fig. 8) is split in two $N_S = 4^n$ segments for quantization noise reduction through oversampling, two N_G samples covering non-linear regions at ramp ends, and N_R samples between the N_S segments to improve the slope measurement accuracy. T_m is chosen with $n = 4$ bit from oversampling and a high $V_C = 2V_{pp}$ to reduce quantization noise. Other T_m may require higher I values, which may lower the frontend sensitivity (see Fig. 9). The

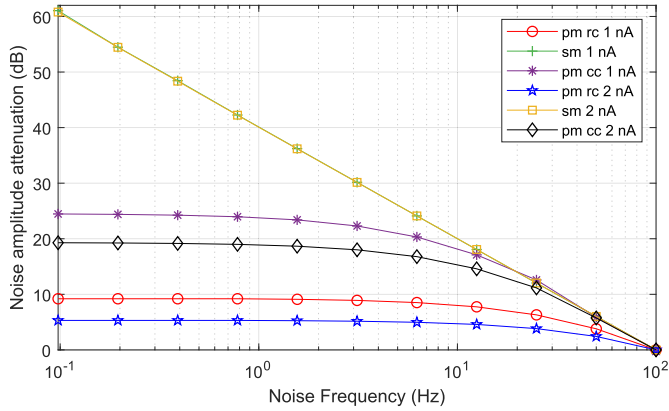


Fig. 11. Drift noise attenuation by slope modulation (sm), constant current period modulation (pm cc), and RC period modulation (pm rc) frontends for frequencies 0.1 Hz to 100Hz and amplitudes 1 nA and 2 nA.

parameters should be optimized when the plate capacitance changes significantly, e.g., for different plate dimensions.

For better comparison, the constant current period modulation frontend uses the same current, $I = 40$ nA, and measurement period, $T_m = 1$ ms. However, the RC period modulation frontend must use higher average currents (and oscillation frequencies around $f_m \approx 2200$ Hz) for practical R values.

The drift noise in simulation and experiments is modeled using a Howland [30] (see Fig. 7) voltage controlled current generator. The errors induced on capacitance measurement by frontends are measured for 3 decade frequencies, 100 Hz to 0.1 Hz (the low end relevant for drift rejection analysis), and amplitudes 1 nA (the lowest reliably distinguishable from noise) and 2 nA.

B. Simulation Results

Using the parameters discussed in Section IV-A, drift noise rejection of all frontends in LTspice [31] simulations are analyzed and compared.

Fig. 11 comparatively shows the noise rejection for all three frontends. The attenuation at low frequencies is plotted against a reference set at a much higher frequency, 100 Hz. Note that for the slope modulation frontend the quantization error from the 12 hardware bits of the ADC and the 4 bits obtained from oversampling and decimation (see Section IV-A) is also implemented in simulation. For the period modulation frontends we use instead the double precision numerical representation of the simulator.

Above a certain frequency, the rejection of all frontends decreases linearly with the increase of the noise frequency. Below that, the rejection of both period modulation frontends has an inflection (at higher frequencies for the RC period modulation frontend), beyond which the noise rejection flattens. This is because these frontends have limited attenuation for constant (dc) drift currents (as discussed in Section II, it is lower for the RC period modulation), which becomes dominant. However, noise attenuation of the slope modulation frontend remains inversely proportional to frequency, according to the theoretically infinite attenuation of constant (dc) noise (see Section II).

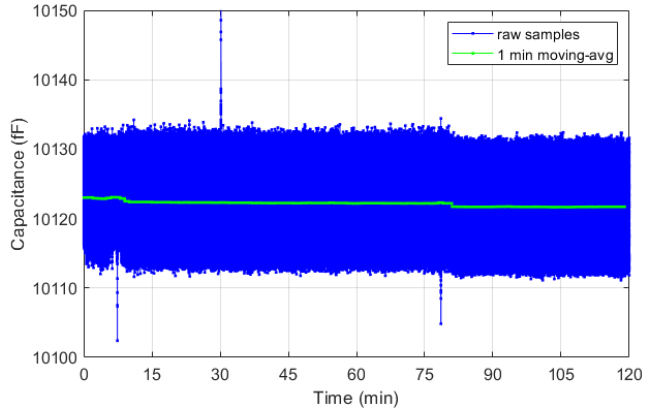


Fig. 12. Stability of the mean value of capacitance for two hours of acquisition of the slope modulator frontend with a fixed capacitor of 10 pF.

It can be also noticed that low frequency attenuation of period modulation frontends (in the flattened zone) depends on noise amplitude. This is because the attenuation of constant (dc) noise depends on the intensity of the noise current (ε_1 in Section II).

C. Experimental Results

The analytical and simulation results are tested experimentally using implementations of the frontends and noise generator. The stability of the current source is important for both the slope modulator and constant current period modulator frontends. The circuit in Fig. 8 is used for both. It operates in uncontrolled environmental conditions (temperature, humidity, ...) without compensations, with the sensor plate replaced by a constant 10 pF capacitor, supplied at 3.3 V by an REF2033AIDCCR [32] accurate voltage regulator providing both the supply and the half-reference voltages (see Fig. 10). The measurement is stable over extended time periods as shown in Fig. 12.

After checking the stability, the frontends are first characterized using a lumped capacitor instead of the sensor plate to reduce the uncontrolled environmental noise. For practical reasons, the frequency range is limited from 25 Hz down to the lowest frequency where the injected noise can be distinguished from the total measurement noise (low frequencies are the most interesting for analyzing drift noise rejection of the frontends).

Fig. 13 shows comparatively both the experimental (dashed line) and the simulation (solid line) results for all three frontends, for a drift noise amplitude of 1 nA. As mentioned above, the new reference is the attenuation at 25 Hz instead of the attenuation at 100 Hz that is used in the simulation results in Fig. 11. Albeit noisier, the experimental results follow closely the simulation results. They reproduce the inflection and flattening behavior for the period modulation frontends (see Section IV-B), and the proportional increase of the drift noise attenuation with the decrease of the noise frequency (up to 1.56 Hz) of the slope modulation frontend.

Fig. 14 shows the same comparison of the simulation (solid line) and experimental (dashed line) results for all three frontends for a higher drift noise amplitude, of 2 nA. The effects can be measured with better accuracy, thus the experimental

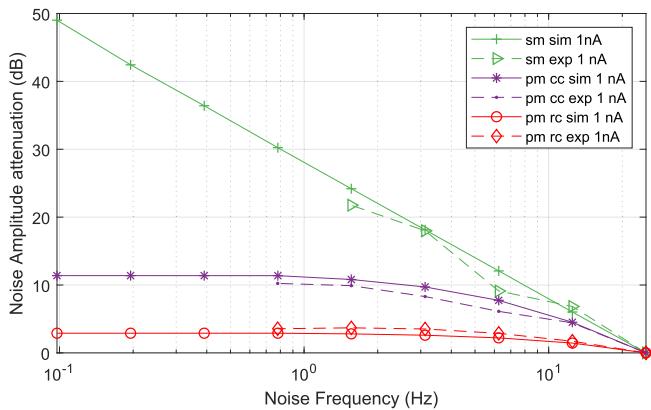


Fig. 13. Simulation and experimental results for the rejection of 1 nA amplitude sinusoidal noise with frequency.

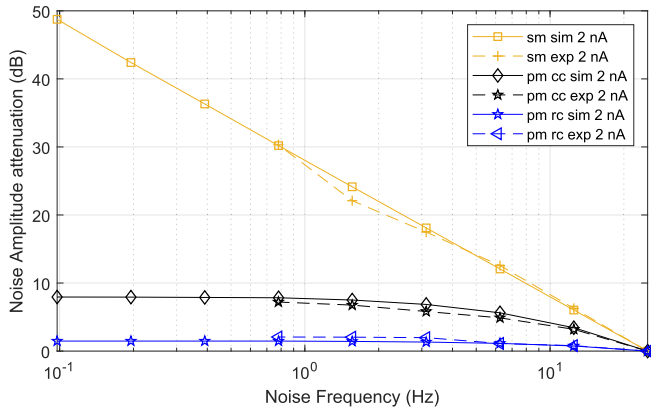


Fig. 14. Simulation and experimental results for the rejection of 2 nA amplitude sinusoidal noise with frequency.

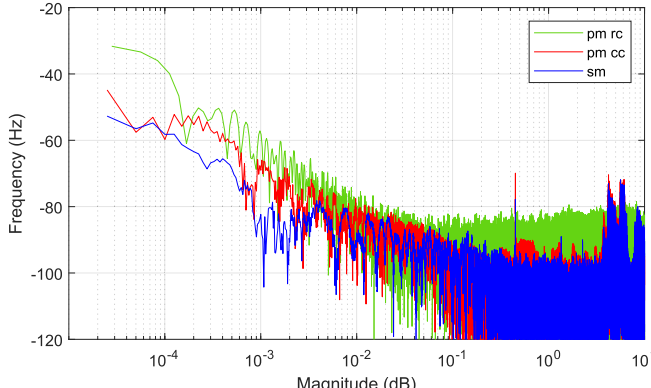


Fig. 15. Frequency analysis of 12 h measurements collected in uncontrolled laboratory conditions by slope modulation (sm), RC period modulation (pm rc), and constant current period modulation (pm cc) frontends.

data match better the simulation results for all frontends, which validates the analytic analysis and the simulation results.

Then the rejection of uncontrolled environmental noise (from sensor circuitry and the environment, electromagnetic, temperature, humidity, etc.) is measured for all frontends. A 16 cm × 16 cm sensing plate is connected to each frontend and measurements for 12 h (from 6:30 PM to 6:30 AM) are collected in the laboratory room. The frequency analysis results are shown in Fig. 15. The expected inflection point below which the 1/f noise becomes dominant can be seen for all frontends. The RC period modulation frontend is the noisiest over the whole spectrum, it has the inflection point at the lowest frequency (around 0.05 Hz), and the highest noise

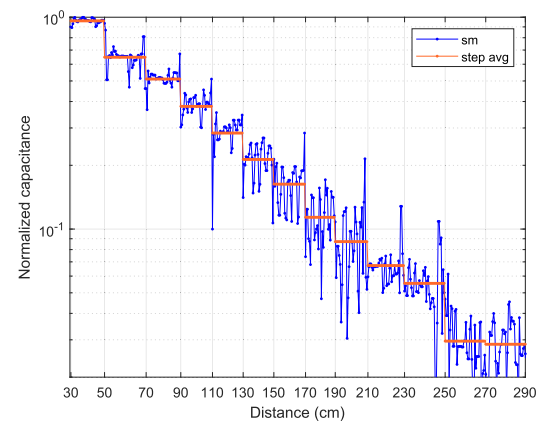


Fig. 16. Plate capacitance measured 4 times/s with the slope modulation frontend for body-plate distances changing by 20 cm every 10 s.

power below that. The constant current period modulation frontend has lower noise power at higher frequencies, the inflection point at a higher frequency (around 0.25 Hz), and shows an improved noise attenuation around 0.01 Hz and below. The slope modulation frontend has comparable noise envelope at higher frequencies and an inflection point roughly at the same frequency, yet the best noise attenuation at lower frequencies.

Although this is beyond the scope of the comparison of the frontend intrinsic performance, it can be noticed that unlike for the period modulation frontends, for the slope modulation frontend an antialiasing filter can be included before the ADC to further improve noise rejection, as shown in Fig. 5.

V. SENSITIVITY CHARACTERIZATION

Sensor noise is usually directly correlated to sensor sensitivity. Thus, it must be checked if a higher sensitivity is in fact the cause of the higher noise of the period modulation frontends.

The frontend noise is evaluated through two main parameters. First, the level below which the person movements produce no discernible changes of the frontend readings. Second, the stability of the frontend readings while the person remains still at various distances in front of the sensor.

For these experiments, the input of each frontend is connected to a 16 cm × 16 cm copper plate, mounted at chest level and several meters away from the surrounding objects. The person stations 10 s in each position, spaced 20 cm along a straight path orthogonal to the plate, at distances from 290 cm to 30 cm. The three frontends are characterized in sequence, in the same conditions, all sampling at 4 sample/s, which is suitable for monitoring indoor person movements [33].

Fig. 16 shows the sensitivity characterization for the slope modulation frontend, as the logarithm of the normalized capacitance on the Y axis function of the distance between the person and the sensor plate on the X axis. Capacitance is normalized for better comparison between frontends, because the absolute values depend on uncontrolled stray capacitances from PCB and components. The average of the readings is also drawn for each stationary position of the person to reduce the influence of the noise. The top of the scale is set at 0.1% higher than the highest average level, and the bottom of the scale at 0.1% lower than the lowest average level.

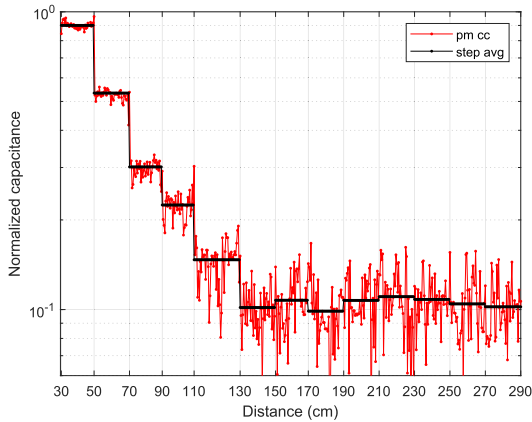


Fig. 17. Sensor capacitance measured 4 times/s with the constant period modulation frontend for body-sensor distances changing 20 cm every 10 s.

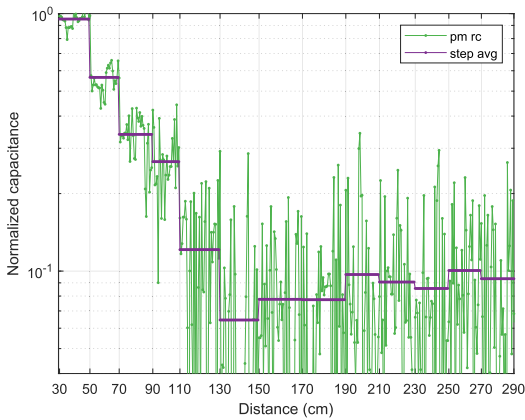


Fig. 18. Sensor plate capacitance measured 4 times/s with the RC period modulation frontend for body-sensor distances changing by 20 cm every 10 s.

First, it can be observed that the sensitivity of the slope modulation frontend extends up to 230 cm, about 10 times the diagonal of the sensor plate. Second, the plate capacitance decreases linearly (on logarithmic scale) with the distance for the whole sensitivity range. This indicates a power dependence of capacitance on the distance to the person, in line with other empirical results in the literature [34]. Third, barring spikes when the person changes position, the measurement noise markedly increases beyond 130 cm, and around 250 cm it exceeds the signal.

Fig. 17 shows the results for the constant current period modulation frontend. For better comparison, it uses similar settings and considerations as Fig. 16. A quasi-linear capacitance-distance dependence (on logarithmic scale) is characterizing up to 90 cm–110 cm. Noise visibly afflicts measurements beyond 110 cm and shortly after it limits the sensitivity.

Fig. 18 shows the results for the experimental evaluation of the sensitivity of the RC period modulation frontend, using similar settings and considerations as Fig. 16 and Fig. 17. The linear capacitance-distance dependence (on logarithmic scale) is visible also here up to 90 cm–110 cm. Noise markedly afflicts the readings beyond 90 cm, then quickly limits the sensitivity.

The experimental sensitivity characterizations show that the slope modulation frontend is the least afflicted by noise, thus

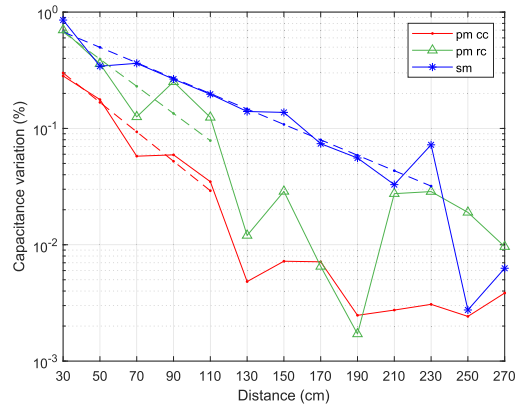


Fig. 19. Frontend sensitivity function of person distance for slope modulation (sm) and period modulation [using RC (pm rc) and constant current (pm cc)].

extending the sensing range to become roughly twice as large as the frontends based on period modulation. The latter are more afflicted by noise, which limits early their sensing ranges as well as the accuracy at closer distances, especially for the RC period modulation frontend.

Fig. 19 comparatively shows the frontend sensitivities calculated as the absolute value of the capacitance reading variation between two adjacent person positions. For all frontends, the sensitivity decreases exponentially with the distance (linearly on logarithmic scale) until it abruptly drops at noise level. The period modulation frontend sensitivities decrease faster and are limited earlier by the higher noise level. Instead, the sensitivity of the slope modulation frontend decreases more slowly and is limited by noise at a much longer sensing distance.

Overall, the experimental results show that the slope modulation frontend is less afflicted by noise and has higher sensitivity, thus longer sensing range than the period modulation frontends.

VI. CONCLUSION AND FUTURE WORK

Environmental drift noise can affect the measurement stability of single plate capacitive sensors used in loading mode for long-time long-range environmental monitoring. Based on a measurement principle similar to period modulation frontends and comparable processing complexity, a slope modulation frontend can effectively reject drift noise for single plate capacitive sensors without sensitivity loss. Moreover, the overall lower noise level notably extends the sensing range of the slope modulator frontends (≈ 230 cm) compared to period modulation frontends (90 cm to 110 cm) using the same 16 cm \times 16 cm sensor plate. Additionally, the slope modulation frontends are compatible with antialiasing filters, further reducing the noise.

These features make frontends based on slope modulation more suitable for long term indoor monitoring of persons using small size sensors that are easier to conceal to avoid discomfort and reduce cost, e.g., in assisted living applications.

Neural network architectures designed to infer the dynamics of the human body movements can be explored in the future to improve the results and verify if they can further reduce the noise.

REFERENCES

- [1] V. Rantanen, P.-H. Niemenlehto, J. Verho, and J. Lekkala, "Capacitive facial movement detection for human-computer interaction to click by frowning and lifting eyebrows," *Med. Biol. Eng. Comput.*, vol. 48, no. 1, pp. 39–47, Jan. 2010.
- [2] F. Reverter, X. Li, and G. C. M. Meijer, "Liquid-level measurement system based on a remote grounded capacitive sensor," *Sens. Actuators A, Phys.*, vol. 138, no. 1, pp. 1–8, Jul. 2007.
- [3] Y. Liu, J. Deng, Y. Ye, C. Han, Z. Hou, and Z. Duan, "Capacitive sensor for vehicle obstacle detection, especially for pedestrian detection," *Microsyst. Technol.*, vol. 26, no. 4, pp. 1179–1186, Oct. 2019.
- [4] T. Grosse-Poppendahl *et al.*, "Finding common ground: A survey of capacitive sensing in human-computer interaction," in *Proc. CHI Conf. Hum. Factors Comput. Syst.*, May 2017, pp. 3293–3315.
- [5] S. Laflamme, M. Kollosche, J. J. Connor, and G. Kofod, "Soft capacitive sensor for structural health monitoring of large-scale systems," *Struct. Control Health Monitor.*, vol. 19, no. 1, pp. 70–81, Feb. 2012.
- [6] Y. Zhang, R. However, B. Gogoi, and N. Yazdi, "A high-sensitive ultra-thin MEMS capacitive pressure sensor," in *Proc. 16th Int. Solid-State Sensors, Actuator Microsyst. Conf.*, Jun. 2011, pp. 112–115.
- [7] P. Bindra and A. Hazra, "Capacitive gas and vapor sensors using nanomaterials," *J. Mater. Sci., Mater. Electron.*, vol. 29, no. 8, pp. 6129–6148, Apr. 2018.
- [8] S. Wöckel, U. Hempel, and J. Auge, "Acousto-capacitive tomography of liquid multiphase systems," *Sens. Actuators A, Phys.*, vol. 172, no. 1, pp. 322–329, Dec. 2011.
- [9] A. Kakimoto, "Detection of surface defects on steel ball bearings in production process using a capacitive sensor," *Measurement*, vol. 17, no. 1, pp. 51–57, Jan. 1996.
- [10] Y. Bai, I. D. Nevelin, M. Peshkin, and M. A. MacIver, "Enhanced detection performance in electrosense through capacitive sensing," *Bioinspiration Biomimetics*, vol. 11, no. 5, Aug. 2016, Art. no. 055001.
- [11] O. B. Tariq, M. T. Lazarescu, J. Iqbal, and L. Lavagno, "Performance of machine learning classifiers for indoor person localization with capacitive sensors," *IEEE Access*, vol. 5, pp. 12913–12926, 2017.
- [12] J. Iqbal, M. T. Lazarescu, O. B. Tariq, A. Arif, and L. Lavagno, "Capacitive sensor for tagless remote human identification using body frequency absorption signatures," *IEEE Trans. Instrum. Meas.*, vol. 67, no. 4, pp. 789–797, Apr. 2018.
- [13] A. Braun, S. Rus, and M. Majewski, "Invisible human sensing in smart living environments using capacitive sensors," in *Ambient Assisted Living*, Cham, Switzerland: Springer, 2017, pp. 43–53.
- [14] S. A. Lowe and G. ÓLaighin, "Monitoring human health behaviour in one's living environment: A technological review," *Med. Eng. Phys.*, vol. 36, no. 2, pp. 147–168, Feb. 2014.
- [15] J. Boehm, R. Gerber, and N. R. C. Kiley, "Sensors for magnetic bearings," *IEEE Trans. Magn.*, vol. 29, no. 6, pp. 2962–2964, Nov. 1993.
- [16] F. Reverter, X. Li, and G. C. Meijer, "Stability and accuracy of active shielding for grounded capacitive sensors," *Meas. Sci. Technol.*, vol. 17, no. 11, p. 2884, 2006.
- [17] D. Kang, W. Lee, and W. Moon, "A technique for drift compensation of an area-varying capacitive displacement sensor for nano-metrology," *Proc. Eng.*, vol. 5, pp. 412–415, Jan. 2010.
- [18] Z. Tan, S. H. Shalmany, G. C. M. Meijer, and M. A. P. Pertijis, "An energy-efficient 15-bit capacitive-sensor interface based on period modulation," *IEEE J. Solid-State Circuits*, vol. 47, no. 7, pp. 1703–1711, Jul. 2012.
- [19] A. De Marcellis, G. Ferri, and P. Mantenuito, "A CCII-based non-inverting Schmitt trigger and its application as astable multivibrator for capacitive sensor interfacing," *Int. J. Circuit Theory Appl.*, vol. 45, no. 8, pp. 1060–1076, 2017.
- [20] A. A. Bijargah, A. Heidary, P. Torkzadeh, and S. Nihtianov, "An accurate and power-efficient period-modulator-based interface for grounded capacitive sensors," *Int. J. Circuit Theory Appl.*, vol. 47, no. 8, pp. 1211–1224, May 2019.
- [21] A. R. Akhmareh, M. T. Lazarescu, O. B. Tariq, and L. Lavagno, "A tagless indoor localization system based on capacitive sensing technology," *Sensors*, vol. 16, no. 9, p. 1448, 2016.
- [22] F. Reverter and O. Casas, "Interfacing differential capacitive sensors to microcontrollers: A direct approach," *IEEE Trans. Instrum. Meas.*, vol. 59, no. 10, pp. 2763–2769, Oct. 2010.
- [23] N. M. Mohan, A. R. Shet, S. Kedarnath, and V. J. Kumar, "Digital converter for differential capacitive sensors," *IEEE Trans. Instrum. Meas.*, vol. 57, no. 11, pp. 2576–2581, Nov. 2008.
- [24] L. K. Baxter, *Capacitive Sensors: Design and Applications* (Electronics Technology). Hoboken, NJ, USA: Wiley, Sep. 1996.
- [25] M. Kelly, G. Servais, and T. Pfaffenbach, "An investigation of human body electrostatic discharge," in *Proc. Int. Symp. Test. Failure Anal.* Orland Park, IL: Amer. Tech. Publishers, Nov. 1993, p. 167.
- [26] C. E. Shannon, "Communication in the presence of noise," *Proc. IRE*, vol. 37, pp. 10–21, Feb. 1949.
- [27] M. Bjelić, M. Stanojević, J. D. Ćertić, and M. Merkle, "Statistical properties of quantisation noise in analogue-to-digital converter with oversampling and decimation," *IET Circuits, Devices Syst.*, vol. 11, no. 5, pp. 421–427, Sep. 2017.
- [28] D. Marioli, E. Sardini, and A. Taroni, "High-accuracy measurement techniques for capacitance transducers," *Meas. Sci. Technol.*, vol. 4, no. 3, pp. 337–343, Mar. 1993, doi: [10.1088/0957-0233/4/3/012](https://doi.org/10.1088/0957-0233/4/3/012).
- [29] *Datasheet STM32L412xx Ultra-Low-Power Arm® Cortex*. Accessed: Feb. 9, 2022. [Online]. Available: <https://www.st.com/resource/en/datasheet/stm32l412kb.pdf>
- [30] Texas Instruments. *Comprehensive Study of the Howland Current Pump*. Accessed: Feb. 9, 2022. [Online]. Available: <https://www.ti.com/lit/pdf/sn0474>
- [31] Analog Devices. *LTspice Simulator*. Accessed: Feb. 9, 2022. [Online]. Available: <https://www.analog.com/en/design-center/design-tools-and-calculators/lts spice-simulator.html>
- [32] *REF2033 3.3-V Vref, Low-Drift, Low-power, Dual-Output Vref & Vref2 Voltage Reference*. Accessed: May 16, 2022. [Online]. Available: <https://www.ti.com/product/REF2033>
- [33] E. M. Diaz, O. Heirich, M. Khider, and P. Robertson, "Optimal sampling frequency and bias error modeling for foot-mounted IMUs," in *Proc. Int. Conf. Indoor Positioning Indoor Navigat.*, Oct. 2013, pp. 1–9.
- [34] R. Wimmer, M. Kranz, S. Boring, and A. Schmidt, "A capacitive sensing toolkit for pervasive activity detection and recognition," in *Proc. 5th Annu. IEEE Int. Conf. Pervasive Comput. Commun. (PerCom)*, Mar. 2007, pp. 171–180.



Giorgia Subbicini (Member, IEEE) received the M.S. (*cum laude*) degree in computer engineering with specialization in embedded systems from the Politecnico di Torino in 2020, where she is currently pursuing the Ph.D. degree in electrical, electronics and telecommunications engineering. She is working on capacitive sensors, indoor localization, and machine learning.



Luciano Lavagno (Senior Member, IEEE) received the Ph.D. degree in EECS from the University of California at Berkeley, Berkeley, CA, USA, in 1992. Since 1993, he has been a Professor with the Politecnico di Torino, Italy. He was the Architect of the POLIS HW/SW co-design tool. From 2003 to 2014, he was an Architect of the Cadence CtoSilicon high-level synthesis tool. He coauthored four books and over 200 scientific articles. His research interests include synthesis of asynchronous circuits, HW/SW co-design, high-level synthesis, and design tools for wireless sensor networks.



Mihai T. Lazarescu (Senior Member, IEEE) received the Ph.D. degree in electronics and communications from the Politecnico di Torino, Italy, in 1998. He was a Senior Engineer at Cadence Design Systems and founded several startups. He works now as an Associate Professor with the Politecnico di Torino. He coauthored more than 60 scientific publications, four books, and several international patents. His research interests include design tools for the reusable WSN/IoT platforms, low-power sensing, neural networks, embedded design, indoor human localization, the distributed IoT data processing, and high-level HW/SW co-design and synthesis.